International Journal of Heat and Fluid Flow 000 (2017) 1–11

Contents lists available at ScienceDirect

International Journal of Heat and Fluid Flow

journal homepage: www.elsevier.com/locate/ijhff

The combined effect of electric forces and confinement ratio on the bubble rising

A. Rahmat[a,b], N. Tofighi[a,b], M. Yildiz[a,b,c,*]

[a] Faculty of Engineering and Natural Sciences, Sabanci University, Tuzla, 34956 Istanbul, Turkey
[b] Integrated Manufacturing Technologies Research and Application Center, Sabanci University, Tuzla, 34956, Istanbul, Turkey
[c] Sabanci University-Kordsa Global, Composite Technologies Center of Excellence, Istanbul Technology Development Zone, Sanayi Mah. Teknopark Blvd. No: 1/1B, Pendik, 34906 Istanbul, Turkey

ARTICLE INFO

Article history:
Received 7 September 2016
Revised 22 December 2016
Accepted 5 January 2017
Available online xxx

Keywords:
Multiphase flows
Confinement ratio
Numerical simulations
VOF method
Bubble dynamics
Electrohydrodynamics (EHD)

ABSTRACT

In this work, the combined effect of electrohydrodynamic forces and domain confinement on the formation of a toroidal bubble is numerically studied. The numerical scheme is the Volume of Fluid (VOF) method and the surface tension and electric forces are implemented using the Continuum Surface Force (CSF) and leaky dielectric models, respectively. It is found that both domain confinement and electric forces are influential on the formation of a toroidal bubble. For smaller confinement ratios, larger electric forces are required to pierce the bubble. Moreover, the influence of both electric forces and confinement ratio are presented and discussed for bubble vertical velocity, terminal Reynolds number, velocity streamlines and side-wall shear stress.

1. Introduction

The motion of a lighter fluid with a continuous interface in another heavier fluid due to the gravitational force is known as the bubble rising. In addition to numerous natural phenomena, there are plenty of industrial applications such as liquid separation and waste-water treatments (Takahashi et al., 1979; Al-Shamrani et al., 2002), nucleate pool boiling (Yoon et al., 2001) and chemical reactions (Pigeonneau, 2009) where the bubble rising is frequently observed. In most of these applications, the bubble rising is normally accompanied by the deformation of the bubble due to external, environmental and geometrical parameters. Numerous studies have been carried out to investigate the effect of various parameters on the regimes of bubble rising. Clift (Clift et al., 1978) reviewed the bubble rising and illustrated that the motion of the bubble can be categorized by three dimensionless numbers, namely the Reynolds, Morton, and Eotvos numbers which the later can also be referred to as the Bond number. He showed that in small Reynolds and Bond numbers, the bubble remains spherical, but increments of both Reynolds and Bond numbers yield different bubble regimes such as elliptical and spherical caps, as well as ellipsoidal and wobbling shapes. Further investigations (Chen et al., 1999; Bonometti and Magnaudet, 2006; Han et al., 2010; Hua and Lou, 2007) revealed that bubbles may deform to a toroid under sufficiently large magnitudes of Reynolds and Bond numbers.

Chen et al. (1999) studied the bubble deformation and its rise for variations of Reynolds, Bond, density and viscosity ratios, and observed that the transition from an elliptical cap to a toroid is facilitated by means of a jet at the wake of the bubble. They concluded that such a transition occurs in density ratios of greater than 5, but the viscosity ratio does not have a significant effect on the bubble shape and velocity. They also realized that a toroidal bubble always travels slower than an elliptical or mushroom-shaped bubble. Bonometti and Magnaudet (2006) investigated the transition from a spherical cap to a toroidal bubble and realized that the transition takes place by means of two different scenarios. In the first scenario, they mentioned that for large Reynolds numbers, an upward liquid jet is driven by the hydrostatic pressure difference between the two poles of the bubble. If surface tension can not compete with the force due to the upward jet current, the bubble is pierced. The piercing occurs at the Bond number $32 \leq Bo \leq 35$. The piercing due to the second scenario occurs in the absence of surface tension force. If the viscous effects are not sufficiently strong to sustain the local pressure maximum at the bubble front, a toroidal bubble is formed. The second scenario is found to take place in Reynold number $79 \leq Re \leq 84$. Later, Hua and Lou (2007) numerically studied the bubble rising and reported that for constant magnitudes of Reynolds, Bond, density and viscosity

* Corresponding author.
E-mail address: meyildiz@sabanciuniv.edu (M. Yildiz).

http://dx.doi.org/10.1016/j.ijheatfluidflow.2017.01.002

ratios, a toroidal bubble is more likely to be formed when the bubble has an initial prolate shape compared to an initially oblate one. Nonetheless, these bubble regimes can also be affected by other parameters such as external forces and domain constraints.

The electrohydrodynamics (EHD), the imposition of electrical forces on fluid flow problems, is one of the means of manipulating flow regimes in bubble rising problems. Mählmann and Papageorgiou (2009) studied the electrified bubble rising in a two-dimensional space for spherical and ellipsoidal rising regimes under the assumption of perfect dielectric model. They revealed that the bubble initially deforms to a prolate shape and later changes to an oblate shape performing "wobbly-like" oscillations. They also showed that the EHD effects increase the vertical rise velocity of the bubble. Wang et al. (2015) simulated the influence of EHD effects on bubble rising and showed that increments of the electric field strength has a direct relationship with the deformation of bubble. They also illustrated that further increments of electric field lead to the formation of a toroidal shape.

Also, the domain constraints have a significant effect on the bubble morphology. Mukundakrishnan et al. (2007) investigated the effect of domain confinement in a two-dimensional axisymmetric geometry on the bubble rising. They realized that the vertical and horizontal confinements are important when the domain height and width are smaller than 8 and 3 times of the bubble diameter, respectively. Recently, Kumar and Vanka (2015) studied the effect of domain confinement on bubble dynamics in a square duct for Bond number ranges of 1 – 100 and three confinement ratios and realized that for Bond number of 1, the bubble does not deform and corresponding aspect ratios (the ratio of vertical bubble diameter over its horizontal diameter) are independent of confinement and Reynolds number. For higher Bond numbers, however, the deformation is significant and the aspect ratio increases by incrementing both Bond number and confinement ratio. Nevertheless, the combined effect of the external electric forces on the bubble dynamics during its rising in a confined domain and possible influence of the EHD effects on the on the formation of a toroidal bubble has not been studied yet.

In this paper, the combined effect of external electric force and confinement ratio on the formation of a toroidal bubble is numerically investigated. In Section 2, the governing equations and dimensionless parameters are presented. In Section 3, the computational domain and relevant boundary conditions are introduced. Moreover in Section 3, the numerical tool is validated by comparing the results with some of those available in the literature, and the dependency of the results with respect to the grid resolution is tested. In Section 4, the results are provided and the combined effect of electrical Capillary and confinement ratio on the formation of a toroidal bubble is discussed. Finally, the concluding remarks are presented in Section 5.

2. Governing equations and numerical scheme

Equations governing an incompressible flow may be written as

$$\nabla\cdot\mathbf{u}=0, \tag{1}$$

$$\rho\frac{\mathrm{D}\mathbf{u}}{\mathrm{Dt}}=-\nabla p+\frac{1}{\mathrm{Re}}\nabla\cdot\mathbf{T}+\frac{1}{\mathrm{Bo}}\mathbf{f}_{(s)}+\frac{1}{\mathrm{Eg}}\mathbf{f}_{(e)}, \tag{2}$$

where $\mathbf{u}$ is the velocity vector, p is pressure, ρ is density, t is time and $\mathrm{D}/\mathrm{Dt}=\partial/\partial\mathrm{t}+\mathbf{u}\cdot\nabla$ represents the material time derivative. In this study, normal letters indicate scalar quantities and bold letters represent vectors and tensors. Here, $\mathbf{T}$ is the viscous stress tensor,

$$\mathbf{T}=\mu\left[\nabla\mathbf{u}+(\nabla\mathbf{u})^{\dagger}\right], \tag{3}$$

where μ denotes viscosity and superscript $\square^{\dagger}$ represents the transpose operation. Local surface tension force is expressed as an equivalent volumetric force according to the continuum surface (CSF) method (Brackbill et al., 1992),

$$\mathbf{f}_{(s)}=\gamma\kappa\hat{\mathbf{n}}\delta. \tag{4}$$

Here, surface tension coefficient, γ, is taken to be constant while κ represents interface curvature, $-\nabla\cdot\hat{\mathbf{n}}$, where $\hat{\mathbf{n}}$ is unit surface normal vector. $\mathbf{f}_{(e)}$ is the electric force vector defined as (Saville, 1997)

$$\mathbf{f}_{(e)}=-\frac{1}{2}\mathbf{E}\cdot\mathbf{E}\nabla\varepsilon+q^{v}\mathbf{E}. \tag{5}$$

In the above equation, ε denotes electric permittivity, q^v is the volume charge density near the interface while $\mathbf{E}$ is the electric field vector. Assuming small dynamic currents and neglecting magnetic induction effects, the electric field is irrotational Hua et al. (2008) and may be represented by gradient of an electric potential ϕ, $\mathbf{E}=-\nabla\phi$. In the above equation, the electrostrictive force vanishes due to the fact that the system is assumed to be incompressible, thus the electric permittivity does not vary with respect to the fluid density (Eringen and Maugin, 2012). Further assumption of fast electric relaxation time compared to viscous relaxation time leads to the following relations for electric potential and charge density

$$\nabla\cdot\left(\sigma\nabla\phi\right)=0, \tag{6}$$

$$q^{v}=\nabla\cdot\left(\varepsilon\nabla\phi\right), \tag{7}$$

where σ is the electrical conductivity.

Dimensionless values are formed using the following scales

$$\mathbf{r}=\mathbf{r}^{+}/\mathrm{d},\quad \mathbf{z}=\mathbf{z}^{+}/\mathrm{d},\quad \rho=\rho^{+}/\rho_f,\quad \mu=\mu^{+}/\mu_f\quad \mathbf{u}=\mathbf{u}^{+}/\sqrt{\mathrm{gd}},$$
$$\mathrm{t}=\mathrm{t}^{+}\sqrt{\mathrm{g}/\mathrm{d}},\qquad \mathbf{E}=\mathbf{E}^{+}/E_{\infty},\qquad p=\left(p^{+}-\rho\mathbf{g}\cdot\mathbf{x}^{+}\right)/\rho_f\mathrm{gd},$$
$$\mathcal{D}=\rho_b/\rho_f,\qquad \mathcal{V}=\mu_b/\mu_f,\qquad \mathcal{P}=\varepsilon_b/\varepsilon_f,\qquad \mathcal{C}=\sigma_b/\sigma_f, \tag{8}$$

leading to Reynolds, Bond, Electro-gravitational and Electro-capillary numbers defined as

$$\mathrm{Re}=\frac{\rho_f\sqrt{\mathrm{gd}^3}}{\mu_f},\quad \mathrm{Bo}=\frac{\rho_f\mathrm{gd}^2}{\gamma},\quad \mathrm{Eg}=\frac{\rho_f\mathrm{gd}}{\varepsilon_f E_{\infty}^2},\quad \mathrm{Ec}=\frac{\mathrm{Bo}}{\mathrm{Eg}}=\frac{\varepsilon_f E_{\infty}^2\mathrm{d}}{\gamma}. \tag{9}$$

Here d is the bubble diameter, E_{∞} is the undisturbed electric field intensity and g is the gravitational acceleration. A plus sign marks dimensional variables whereas subscripts $\square_b$ and $\square_f$ denote bubble and surrounding fluid phases, respectively.

In the Volume of Fluid (VOF) method, the volume fraction α is calculated by solving an evolution equation as,

$$\frac{\partial\alpha}{\partial t}+\mathbf{u}\cdot\nabla\alpha=0, \tag{10}$$

and fluid properties are smoothed on the interface by,

$$\xi=\alpha\xi_b+(1-\alpha)\xi_f, \tag{11}$$

where ξ can be any physical fluid property such as density, viscosity, electrical conductivity or permittivity whichever is appropriate.

In this paper, the finite volume method is used to discretize the continuity and momentum equations. The momentum equation (Eq. 2) is solved by a second-order upwind formulation both in time and space. The PRESTO! method is employed to calculate the pressure field, and the pressure and velocity fields are coupled using the SIMPLE scheme.

The commercial ANSYS Fluent software is used to solve the relevant governing equations together with the associated boundary conditions. In addition to the continuity and momentum equations, a Laplace equation needs to be solved to obtain the electric field (Eq. 6) in the domain. This has been carried out using a User Defined Function (UDF). Then, the electric field is evaluated as the

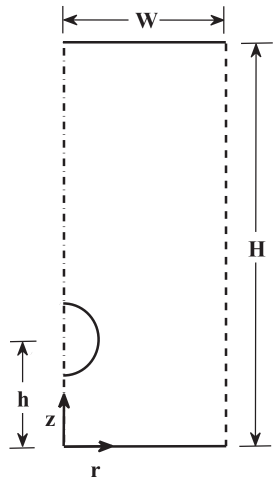

Fig. 1. Schematic of the test case.

gradient of the electric potential in the entire domain and relevant forces are calculated using Eqs. 5 and 7. Then the forces are added as a source term to the momentum equation.

3. Problem setup

3.1. Geometry and boundary conditions

In this study, the axisymmetric simulation domain is a rectangle with a height of H and width of W wherein the bubble is centered at a distance of $h = 4(d/2)$ from the bottom boundary, as shown schematically in Fig. 1. The domain height is set to $H = 24(d/2)$ which is tested in the preliminary studies ensuring the system to be independent from vertical boundary confinement. The width of the domain is adjusted accordingly to maintain the desired confinement ratio. No-slip condition along with a potential difference of $\Delta\phi = E_\infty/H$ is applied to top and bottom walls shown by solid lines in Fig. 1. Referring to Fig. 1, the left and right boundaries are shown with dash-dot and dash lines representing the domain axis and the side wall, respectively. The right boundary abides the no-slip boundary condition and a Neumann boundary condition for the electric potential. In the absence of the bubble, this produces a uniform downward electric field parallel to the side walls. In all simulations including the validation and convergence tests, the time step is set to keep the Courant–Friedrichs–Lewy (CFL) condition below 0.2 (CFL $<$ 0.2).

3.2. Validation and resolution study

To validate the results of present study, three test cases (VT1, VT2 and VT3) are simulated and compared with those from experiments of Bhaga and Weber (1981) and numerical findings of Hua and Lou (2007). In order to ensure that the results are not affected by the side wall effects, the diameter and height of the axisymmetric domain is taken six and twelve times larger that the bubble diameter ($W = 6(d/2)$) and ($H = 24(d/2)$), respectively. The bubble is located at a distance of two bubble diameter from the bottom boundary, and the boundary conditions are similar to those indicated in Fig. 1. The simulation condition of the test case VT1 is [$Re = 33.02$, $Bo = 116$], while VT2 and VT3 cases have simulation conditions of [$Re = 135.4$, $Bo = 116$], and [$Re = 15.24$, $Bo = 243$], respectively, and the density and viscosity ratios are $\mathcal{D} = 1000$, $\mathcal{V} = 100$. These conditions are identical to those of Hua and Lou (2007) and equivalent with results of Bhaga and Weber (1981). It should be noted that in Bhaga and Weber (1981) the Reynolds number is calculated based on the terminal rise velocity (U_t) of the bubble and named as the terminal Reynolds number $Re^* = \rho_f U_t d/\mu_f$. Table 1 compares terminal bubble shapes and vertical rise velocity of VT1, VT2 and VT3 with experiments in Bhaga and Weber (1981) and simulations in Hua and Lou (2007). Considering terminal bubble shapes, the present numerical results are satisfactory in general, and matches with results of the provided references. The comparison of terminal rise velocity with numerical simulations in Hua and Lou (2007) shows that the present numerical results underestimates the vertical rise velocity for VT2 and VT3 by the relative difference of 0.9% and 1.6%, respectively, and overestimates the rise velocity of VT1 by the relative difference of 1.8%.

There is a difference observed between the characterized Reynolds number (Re) of numerical simulations and calculated Reynolds number (Re^*) of experimental studies. Based on the dimensionless and characteristic parameters, the terminal rise velocity of the bubble can be found by $U_t.\sqrt{gd}$, and the Reynolds number calculated based on the dimensional terminal rise velocity can be obtained by $Re_c^* = U_t.Re$. For the above simulated cases, the calculated Reynolds number is found to be $Re_c^* = 20.24$, $Re_c^* = 88.55$ and $Re_c^* = 8.26$ for cases VT1, VT2, and VT3 which shows relative difference ($\frac{|Re^* - Re_c^*|}{Re^*} \times 100$) compared to the experimental finding of Bhaga and Weber (1981) by 0.78, 5.8, and 6.3 percentages, respectively. It should be noted that similar comparison has been made by Hua and Lou (2007) reporting comparable results.

Fig. 2 presents the dependency of present numerical results on the grid the resolution for the test case VT3 from Table 1. For all simulations in this paper, the domain is meshed by Cartesian structured mesh model. The test is carried out for four different resolution cases of $MR1 = 24\chi$, $MR2 = 32\chi$, $MR3 = 48\chi$, and $MR4 = 64\chi$, where $n\chi$ indicates the number of grids per initial bubble diameter. It is observed that for the coarse case of MR1, the bubble vertical velocity is under predicted and the bubble shape has considerable distinctions compared to other cases. The comparison of MR3 and MR4 reveals that the increase in the grid resolution does not change the results considerably, thus the resolution of MR3 is adopted for the simulations of the present study. It should be mentioned that the validation of present study in Table 1 are also carried out with the same mesh resolution (MR3).

In order to validate the code for implementation of the electric forces, the deformation of a stationary bubble in a quiescent fluid is simulated. The bubble is located in an axisymmetric domain of ($H = 12(d/2)$) and ($W = 6(d/2)$) where the distance of the bubble center from the top and bottom boundaries are the same. The boundary conditions are also similar to those explained in Fig. 1. The density, viscosity and conductivity ratios are $\mathcal{D} = 1$, $\mathcal{V} = 1$, and $\mathcal{C} = 5$, respectively, and the applied electric potential yields the Electro-capillary number of $Ec = 0.4$. In order to quantify the deformation of the bubble, the deformation index of the bubble D_ι is introduced as the fraction of the difference of bubble vertical (ς) and horizontal (ϱ) diameters over their summation, $D_\iota = (\varsigma - \varrho)/(\varsigma + \varrho)$. The positive values of deformation index indicates the deformation of the bubble in the direction of electric field (prolate deformation) and its negative values represents the deformation perpendicular to the direction of the electric field (oblate deformation). Fig. 3 compares the deformation index of the test case for variations of electric permittivity ratio with Taylor's theory (Taylor, 1966) and numerical results of Lin et al. (2012) for an inviscid system. It can be shown that the bubble deformation index is a weak function of viscosity ratio (Saville, 1997) and variations of viscosity ratio does not change the results, considerably. The Taylor's theory can be simplified for a bubble in an inviscid system as,

$$D_\iota = \frac{9}{32(2+\mathcal{C})^2}\frac{\varphi}{} \frac{\varepsilon_f E_\infty^2 d}{\gamma} = \frac{9}{32(2+\mathcal{C})^2}\frac{\varphi}{} Ec, \tag{12}$$

Table 1
Validation of numerical code with the experiments of Bhaga and Weber (1981) and Hua and Lou (2007) for three test cases; VT1: Re = 33.02 and Bo = 116, VT2: Re = 135.4 and Bo = 116, and VT3: Re = 15.24 and Bo = 243.

Test case	Experiment conditions	Bhaga and Weber (1981)	Simulation conditions	Hua and Lou (2007)	Simulation conditions	Present study
VT1	$Re^* = 20.4$ $Bo = 116$ $U_t = -$	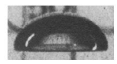	$Re = 33.02$ $Bo = 116$ $U_t = 0.602$		$Re = 33.02$ $Bo = 116$ $U_t = 0.613$	
VT2	$Re^* = 94$ $Bo = 116$ $U_t = -$	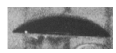	$Re = 135.4$ $Bo = 116$ $U_t = 0.660$		$Re = 135.4$ $Bo = 116$ $U_t = 0.654$	
VT3	$Re^* = 7.77$ $Bo = 243$ $U_t = -$	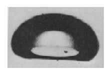	$Re = 15.24$ $Bo = 243$ $U_t = 0.551$		$Re = 15.24$ $Bo = 243$ $U_t = 0.542$	

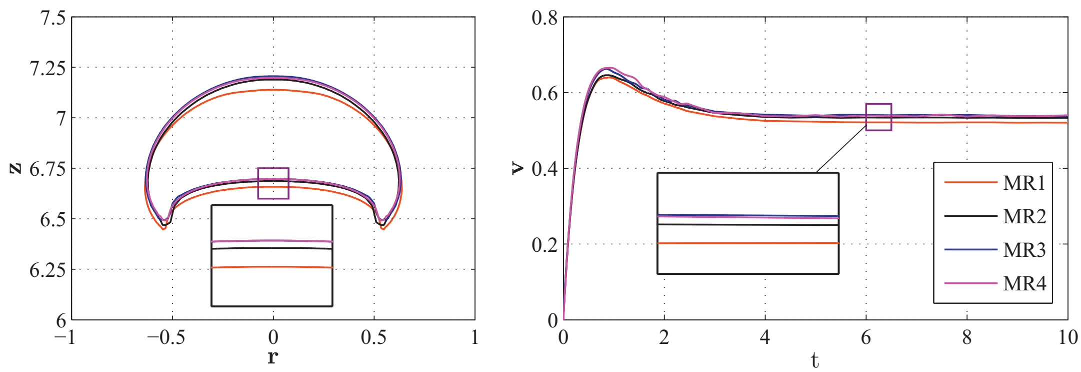

Fig. 2. The grid resolution study for the test case VT3 from Table 1 for bubble shape (at left) and vertical rise velocity (at right), employing four different resolutions of $MR1 = 24\chi$, $MR2 = 32\chi$, $MR3 = 48\chi$, and $MR14 = 64\chi$ where $n\chi$ indicates the number of grids per initial bubble diameter.

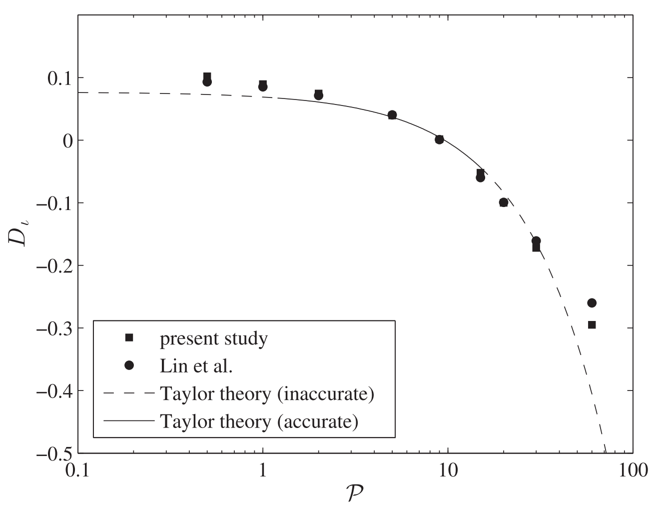

Fig. 3. Comparison the deformation index of present numerical results (square marks) with Lin et al. (2012) (circle marks) and Taylor's theory (Saville, 1997) (dashed and solid lines) for the deformation of a neutrally buoyant bubble; The parameters are set to $\mathcal{D} = 1$, $\mathcal{V} = 1$, $\mathcal{C} = 5$, and $Ec = 0.4$.

where φ is a discrimination function,

$$\varphi = \mathcal{C}^2 + 1 - 2\mathcal{P} + \frac{3}{2}(\mathcal{P} - \mathcal{C}). \tag{13}$$

In Fig. 3, square and circle signs indicate the numerical results of present study and those of Lin et al. (2012), respectively and Taylor's theory is shown with solid and dashed lines. It should be noted that the Taylor's theory gives accurate results for small deformations where the bubble is nearly spherical, but in high deformation cases, the results of the Taylor's theory become inaccurate (Feng and Scott, 1996; Vizika and Saville, 1992; Zhang and Kwok, 2005). Therefore, the dash line illustrates the inaccurate Taylor's theory while the solid lines indicate the region where the theory is accurate. The comparison of the present study with referenced numerical and analytical results illustrates that in the region of small deformation, the deformation index is predicted with a sufficient accuracy. For large oblate deformations, the present results stand between the referenced numerical and analytical results while for the large prolate deformations, the current study slightly overestimates the deformation index compared to both referenced data.

4. Results

In this section, the results of a rising bubble in a cylindrical confined domain under the effect of an external electric field are presented. The domain confinement ratio Cr is defined as the ratio of the diameter of the cylindrical domain over the bubble diameter, $Cr = (2W/d)$. In our preliminary investigations, it is observed that the side wall boundary effects are insignificant for confinement ratios above five ($Cr > 5$). Thus, four confinement ratios of $Cr = 2$, $Cr = 3$, $Cr = 4$, and $Cr = 5$ are considered to take into account the effect of confinement ratio. The simulation conditions of the rising bubble is $Re = 100$, $Bo = 50$, $\mathcal{D} = 0.001$, $\mathcal{V} = 0.01$, $\mathcal{C} = 0.001$, and $\mathcal{P} = 0.05$. Under such simulation conditions and in the absence of electric forces, the bubble deforms to a hemispherical shape in small confinement ratios ($Cr = 2$) due to the effects of the side domain boundaries. By increasing the confinement ratio, the bubble is flattened where the effects of the side domain boundary are lessened. Despite having a wider frontal area, the bubble rises faster in larger confinement ratios. This is a direct consequence of the effects of domain confinement on hydrodynamics of the bubble rising such as the flow vortices inside and outside of the bubble. It should be noted that similar results have been reported in Kumar and Vanka (2015) for equivalent simulation conditions.

It should be noted that the Bond number can also be represented as the ratio of the characteristic length (here the bubble diameter) over the capillary length scale ($l_c = \sqrt{\frac{\gamma}{\rho_f g}}$). In the present study, the characteristic length scale is almost one order of mag-

Please cite this article as: A. Rahmat et al., The combined effect of electric forces and confinement ratio on the bubble rising, International Journal of Heat and Fluid Flow (2017), http://dx.doi.org/10.1016/j.ijheatfluidflow.2017.01.002

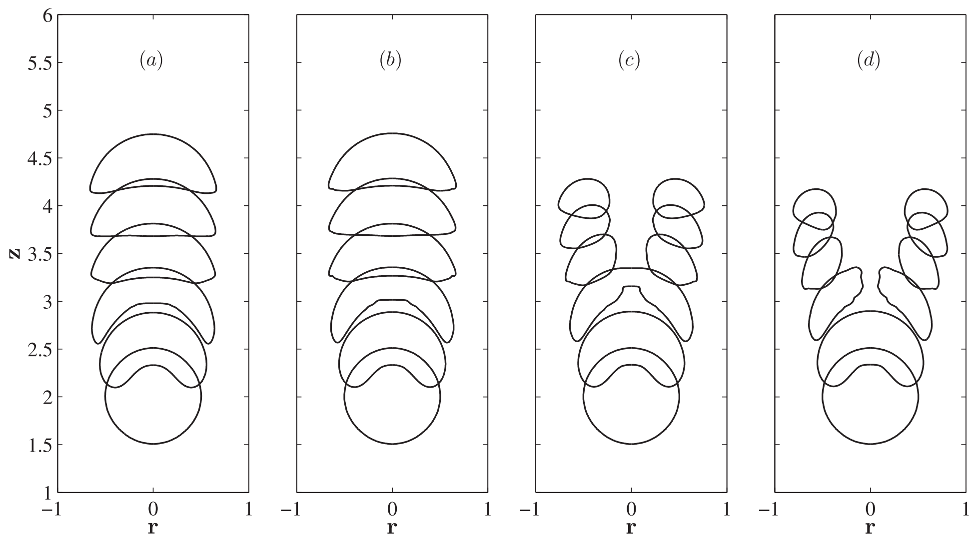

Fig. 4. The history of bubble shapes at $t = 0, 1, 2, 3, 4, 5$ in confinement ratio of $Cr = 2$ for variations of Electro-capillary number; (a) $Ec = 1.0$, (b) $Ec = 1.5$, (c) $Ec = 2.0$, (d) $Ec = 2.5$.

nitude larger that the capillary length scale. This leads to the consideration of just geometrical confinement due to the domain constraints.

In the presence of electric field, the electric potential is adjusted to maintain the Electro-capillary number in the range of $0.5 \leq Ec \leq 2.5$. For small Electro-capillary numbers, $Ec \approx 0.5$, the electric forces does not significantly influence the bubble shape and its vertical rise velocity in any confinement ratio. On the other hand, applying the Electro-capillary number of $Ec = 2.5$ leads to the formation of a toroidal bubble shape for all confinement ratios. In the following, the formation of a toroidal rising bubble is separately investigated for the piercing effect of electric forces in a confined domain, and the influence of confinement ratio in the presence of electric forces. Afterwards, relevant discussions are made on the combined effect of electric forces and confinement ratios on the formation of a toroidal bubble.

4.1. Effect of Ec

Fig. 4 represents the cross-section and the history of bubble shapes at $t = 0, 1, 2, 3, 4, 5$ for the confinement ratio of $Cr = 2$ and for four different Electro-capillary numbers, (a) $Ec = 1.0$, (b) $Ec = 1.5$, (c) $Ec = 2.0$ and (d) $Ec = 2.5$. During the initial transient stage wherein the bubble motion is dominated by inertial force, the bubble deforms from an initial spherical shape to a spherical-cap shape ($t = 2$ in (a) and (b) cases). Here, recall that the initial transient stage refers to dynamics of the bubble from the initial spherical shape to the terminal state of non-pierced cases and to the piercing moment of pierced cases. This deformation is followed by the formation of an upward jet current of the surrounding fluid at the wake of the bubble. Consequently, the bottom surface of the bubble is indented inwardly while the upper surface of the bubble remains nearly spherical. Afterwards, the bubble tries to maintain its terminal shape due to the effect of surface tension where the indentation of the bottom surface is vanished and the bottom surface of the bubble flattens, reaching into a hemispherical state. Increasing the Electro-capillary number in (c) and (d) cases, the bubble is pierced and a toroidal bubble is formed. The piercing occurs when the upward jet current pushes the bottom surface and the distance between the upper and bottom surfaces of the bubble is minimum in the transient stage (notice $t = 2$ in case (c)). At this moment, the electric forces which act on the interface directing into the bubble, facilitate the formation of a toroidal bubble if the magnitude of the Electro-capillary number is sufficiently large. By comparing the bubble shapes at $t = 2$ for (c) and (d) cases in Fig. 4, it is observed that the electric forces pierce the bubble earlier in time in case (d) which has a larger magnitude of the Electro-capillary number. After the bubble is pierced, the surface tension force which is stronger in regions where the curvature is larger, preserves the shape of the bubble ring (notice the deformation of the bubble shape from $t = 2$ to $t = 5$ for case (d)). This can be referred to as the 'secondary transient stage' describing the dynamics of a rising bubble between the piercing moment and reaching its terminal state. Later, it will be discussed how domain confinement affects the secondary transient stage.

In order to see how the electric forces assist the formation of a toroidal bubble, Fig. 5 is presented. In this figure, the normalized electric forces per unit volume are shown at $t = 1$ on the bubble interface for four cases represented in Fig. 4. It is seen that the electric forces increase with increments of Electro-capillary number by comparing the normalized magnitudes of the forces. Considering the distribution of electric forces on the bubble interface, it is observed that the electric forces are stronger on the bottom surface of the bubble. Moreover, the force vectors show that the direction of electric forces are from the heavier fluid towards the lighter one in that region. This shows that when the distance between the upper and bottom surfaces of the bubble are small, the electric forces pierce the bubble from the center.

The vertical rise velocities of cases (a), (b), (c) and (d) from Fig. 4 are presented in Fig. 6. For the initial moments of transient stage nearly up to $t \approx 1$, the vertical rise velocity increases and reaches a maximum, and thereafter decreases due to the distended frontal area which augments the drag force and nearly levels off with relatively small oscillations for non-pierced cases and drops down further for pierced cases. The maximum value of rise velocity gets larger with increments of the Electro-capillary number. This is due to the distribution and direction of electric forces on the bubble interface, as described in Fig. 5. Since the electric forces are stronger on the bottom surface of the bubble during the initial transient stage directing from heavier to lighter fluid, slight increase on the vertical rise velocity is observed for increments of Electro-capillary number. At $t \approx 2$, piercing occurs for $Ec = 2.0$ and $Ec = 2.5$ cases and the upward jet current passes through the pierced area (not shown here), followed by a sudden drop in the vertical rise velocity. As a result, the terminal rise velocity of the pierced bubbles decreases by almost 50 percent compared to

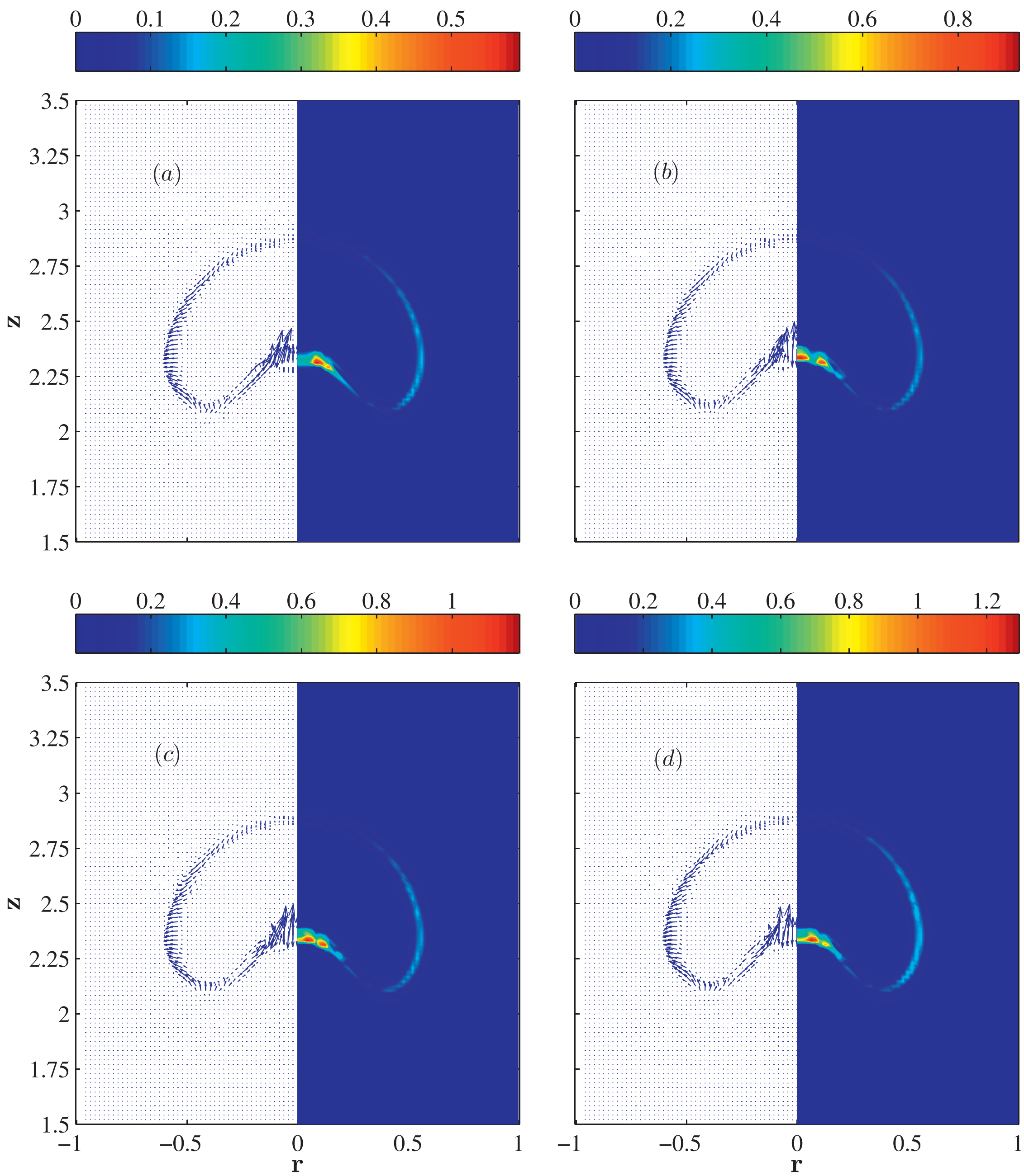

Fig. 5. The electric forces per unit volume normalized by $\varepsilon_f E_n^2/d$ shown by vector field (on the left half) and contours (on the right half) on the interface of the bubble at t = 1 in confinement ratio of Cr = 2 and for (a) Ec = 1.0, (b) Ec = 1.5, (c) Ec = 2.0, (d) Ec = 2.5; In order to compare force magnitudes, the electric field intensity for normalizing the forces E_n is taken equal to 1.

the non-pierced cases. During the secondary transient stage for the pierced cases, the vertical rise velocity decreases slightly from $v \approx 0.4$ to $v \approx 0.3$. This slight decrease is due to the effects of side boundary, and occurs when the bubble ring approaches the side boundaries during its secondary transient stage. For all cases, it is observed that the velocities are oscillatory especially for pierced cases. It will be shown that these oscillations are due to the confinement of the domain and disappear when the confinement ratio is increased.

Fig. 7 represents the velocity streamlines and bubble shapes in the half domain for confinement ratio of Cr = 2 and for different Electro-capillary numbers (Fig. 7(a)–(d)), and their corresponding wall shear stress $\tau = \mu_f \nabla \mathbf{u}|_z$ at the side wall boundary normalized by $\rho_f$gd(Fig. 7(e)). The cases are shown for the moment when the centroid of the bubble is at z = 5. For (a) and (b) cases, the bubble is not pierced, and the velocity streamlines illustrate the structure of the upward jet current at the wake of the bubble. For the pierced cases in (c) and (d), however, no upward jet current of surrounding fluid which passes into the pierced region is observed. It should be noted that after the formation of the toroidal shape, a pair of vortices begin to develop at the sides of the bubble ring. These vortices develop as the bubble rises in the fluid. Simultaneously, the effect of the upward jet current in the pierced region gradually disappears. Consequently, the direction of the surrounding fluid motion in the pierced region is reverted. Such a transformation leads to the formation of some other complex vortices especially beneath the bubble ring. Considering the wall shear stress in Fig. 7(e), it should be noted that positive magnitudes of

Please cite this article as: A. Rahmat et al., The combined effect of electric forces and confinement ratio on the bubble rising, International Journal of Heat and Fluid Flow (2017), http://dx.doi.org/10.1016/j.ijheatfluidflow.2017.01.002

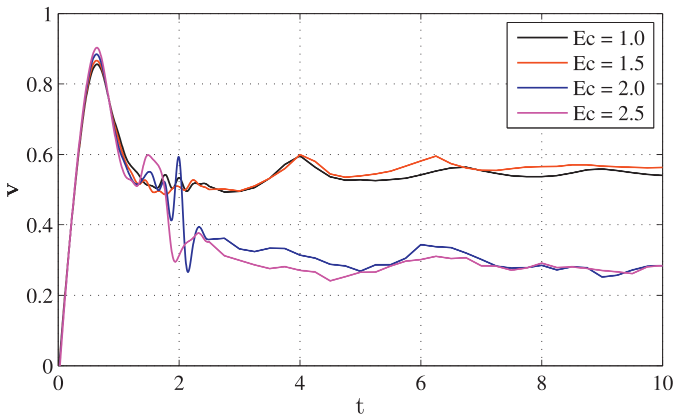

Fig. 6. The vertical rise velocity versus time for constant confinement ratio $Cr = 2$ at different Electro-capillary ratios, $Ec = 1.0, 1.5, 2.0$ and 2.5.

wall shear stress indicate the friction in the upward direction for downward motion of the surrounding fluid at the vicinity of the wall. The maximum value of the wall shear stress slightly increases with increments of Electro-capillary number for non-pierced cases. The location of the maximum value stands at the elevation of the bottom surface of the hemispherical bubble. For the pierced cases, the magnitude of the maximum point increases considerably and its location is at the elevation of the centroid of the bubble ring. Increments of Electro-capillary number for pierced bubbles show a slight decrease in the maximum value of the wall shear stress. For $Ec = 2.5$, the wall shear stress has negative values between $z \approx 3.5$ and $z \approx 4.3$ indicating that an upward current of the surrounding fluid exists in the vicinity of the wall as a direct consequence of the formation of vortices beneath the toroidal bubble.

4.2. Effect of Cr

The cross-section and the history of bubble shapes at $t = 0, 1, 2, 3, 4, 5$ for Electro-capillary $Ec = 1.35$ and various confinement ratios, (a) $Cr = 2$, (b) $Cr = 3$, (c) $Cr = 4$, (d) $Cr = 5$ are shown in Fig. 8. Later it will be shown that how the confinement ratio affects the minimum value of the Electro-capillary number required for piercing the bubble. It will also be shown that in large confinement ratios, there is not much of a difference between the minimum value of Electro-capillary number which can pierce the bubble. Thus, $Ec = 1.35$ is selected to show that the bubble pierces in two larger confinement ratios but remains hemispherical/ellipsoidal in more confined cases. Comparing the bubble terminal shapes for (a) and (b) cases at $t = 5$, it is observed that the bubble is more flattened when the confinement ratio increases, changing the terminal shape from a hemispherical shape in $Cr = 2$ to an ellipsoidal-cap in $Cr = 3$. When the bubble is flattened in larger confinement ratios, the distance between the upper and bottom surface of the bubble in the transient region decreases (notice the bubble shapes at time $t = 2$ and consider the distance between upper and bottom surfaces in $r = 0.0$). Then, the electric forces pierce the bubble from the center forming a toroidal bubble as discussed in Fig. 4. After the formation of the toroidal bubble, the secondary transient stage begins.

Fig. 9 represents the vertical rise velocity versus time for the cases shown in Fig. 8. The maximum value of vertical rise velocity increases with increments of the confinement ratio. This is intuitively expected since the larger the confinement ratio, the less the effect of the no-slip boundary on the rising velocity. Similar to the variations of maximum of vertical rise velocity for different Electro-capillary numbers (Fig. 6), the vertical rise velocity drops down (after $t \approx 1$) due to the enlargement of the frontal area of the bubble and levels off briefly. For (c) and (d) cases, the vertical rise velocity sharply drops down further because of the piercing of bubbles. Further decrease in the vertical rise velocity until $t \approx 5$ for (c) and (d) cases indicates the secondary transient stage of the bubble. After reaching the terminal rise velocity, one can clearly observe the influence of the increments of confinement ratio on the magnitude of the terminal rise velocity for both pierced and non-pierced cases where upon the formation of toroidal bubble,the terminal rise velocity of pierced bubbles falls below those of (a) and (b) cases. It is shown earlier that the vertical rise veloc-

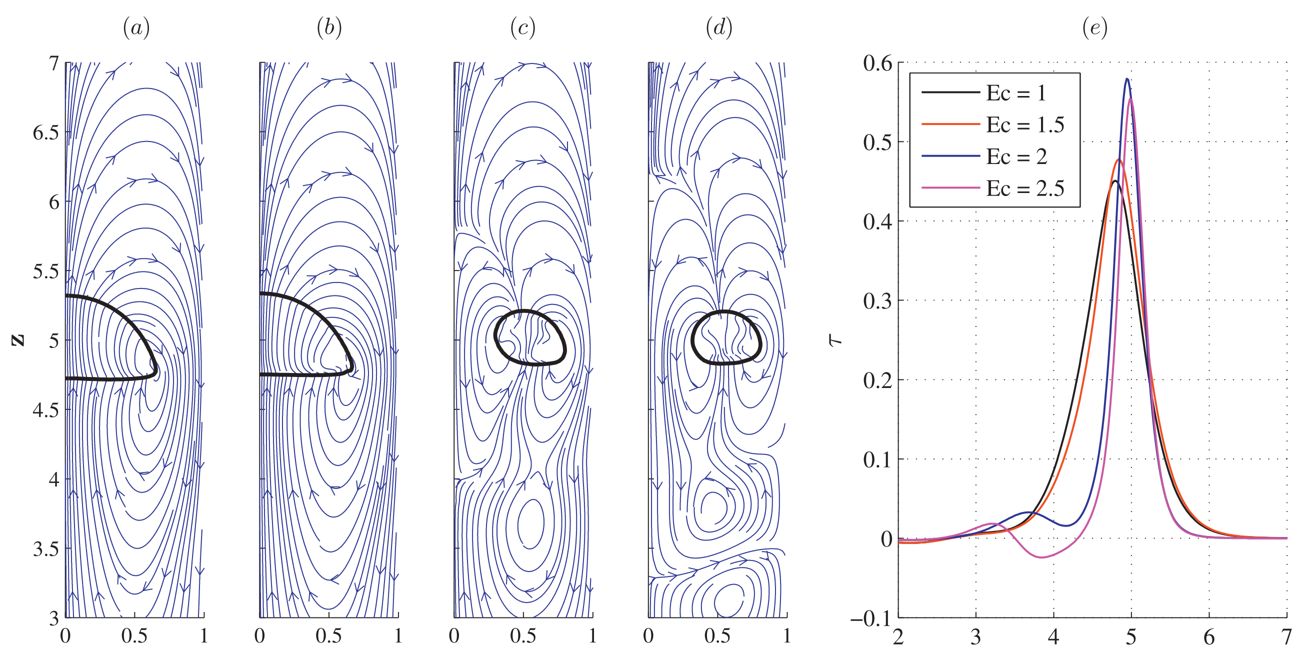

Fig. 7. The velocity streamlines and bubble shapes for confinement ratio for $Cr = 2$ and different Electro-capillary numbers; (a) $Ec = 1.0$, (b) $Ec = 1.5$, (c) $Ec = 2.0$, (d) $Ec = 2.5$ and (e) their corresponding wall shear stress; The bubbles are shown in a half domain for the moment when their centroids are at $z = 5$.

Please cite this article as: A. Rahmat et al., The combined effect of electric forces and confinement ratio on the bubble rising, International Journal of Heat and Fluid Flow (2017), http://dx.doi.org/10.1016/j.ijheatfluidflow.2017.01.002

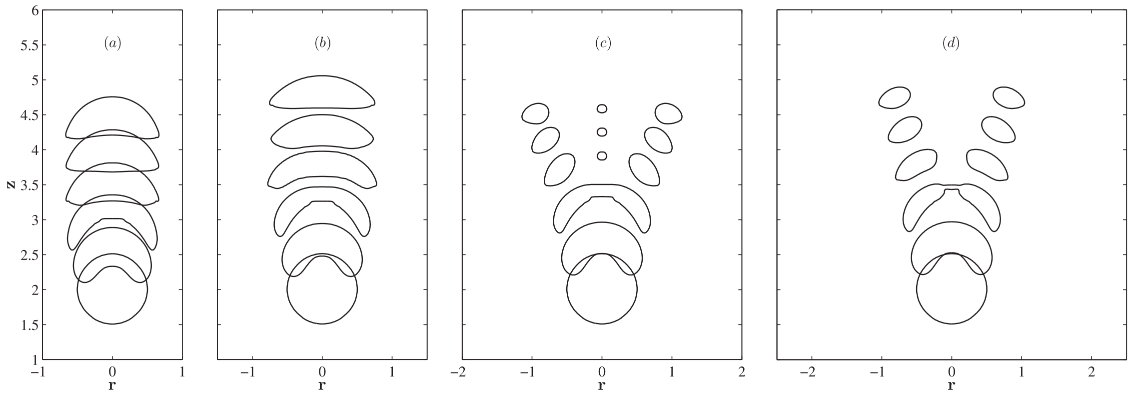

Fig. 8. The history of bubble shapes at t = 0, 1, 2, 3, 4, 5 in Electro-capillary number of Ec = 1.35 for various confinement ratios; (a) Cr = 2, (b) Cr = 3, (c) Cr = 4, (d) Cr = 5.

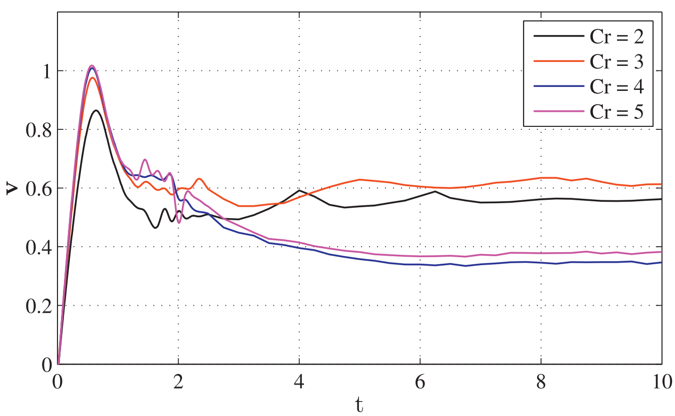

Fig. 9. The vertical rise velocity versus time for constant Electro-capillary numbers Ec = 1.35 at different confinement ratios, Cr = 2, 3, 4 and 5.

ity in small confinement ratios are oscillatory. Here in Fig. 9, it is shown that by increasing the confinement ratio, these oscillations tend to be reduced.

Fig. 10 represents the velocity streamlines and cross section of bubble rings in the half domain for Electro-capillary number of Ec = 2.5 and various confinement ratios (Fig. 10(a)–(d)), and the corresponding side wall shear stress (Fig. 10(e)), at the moment when the centroid of the bubble ring is at z = 5. In relation to the formation of vortices after the piercing of the bubble, it is stated earlier that the jet current of the surrounding fluid gradually disappears after the development of a pair of vortices around the bubble ring. The pair vortices are observable in Fig. 10(a) and (b) at the sides of the bubble interface. However, the development of these vortices depends on the domain confinement. In smaller confinement ratios, the vortices are formed right after the bubble is torn from the center (not shown here), but the formation of vortices are delayed in time for larger confinement ratios. Thus, it is observed in Fig. 10 that for (a) and (b) cases, the vortices are developed and the upward jet current disappears, but the upward jet current passing through the pierced region still exists for (c) and (d) cases. It should be noted that the development of pair vortices around the bubble ring is accompanied by the formation of other vortices beneath the bubble ring. Considering the wall shear stress, its magnitude dramatically increases with decrements of confinement ratio. This represents the effect of side walls on the flow of the surrounding fluid that affects the bubble shape and vertical rise velocity and also the magnitude of Electro-capillary number in which the bubble pierces. Since all the cases are pierced, the maximum values of wall shear stress for all the confinement ratios are in the same location which corresponds to the centroid of the bubble ring. Moreover, it is found that the existence of pair vortices around the bubble ring for Cr = 2 and 3 cases generates negative magnitudes of shear stress on the side wall.

4.3. The combined effect of Cr and Ec

Fig. 11 represents the terminal shapes of bubbles in 3D for different confinement ratios and Electro-capillary numbers at t = 10. For Electro-capillary number of Ec = 1.0, the bubble remains non-pierced for all confinement cases and increments of confinement ratio make the bubble shape flattened. For Ec = 1.5, the bubble keeps its hemispherical shape in Cr = 2, but the bubble is torn when the confinement ratio is increased to Cr = 3. The toroidal shape of the bubble horizontally spreads as the confinement ratio increases to Cr = 4 and 5. Considering larger magnitudes of Electro-capillary number Ec = 2.0 and 2.5, it is observed that the final bubble shape for all confinement ratios is toroidal.

It has shown earlier that both confinement ratio and Electro-capillary number affect the bubble rising regime and have direct influence on the formation of a toroidal bubble (refer to Figs. 8 and 4, respectively). In order to determine the region where the bubble is pierced, a set of simulations in different Electro-capillary numbers and confinement ratios are carried out and the corresponding results are shown in Fig. 12. For four different confinement ratios, various Electro-capillary cases are simulated and the final state of the bubble is indicated by circle and plus marks for the non-pierced and pierced cases, respectively. Moreover, a solid line determines where the bubble shape transforms into a toroidal shape as the Electro-capillary number increases. It is seen that in large confinement ratios Cr = 5, Ec ≈ 1.3 is the threshold value in which a toroidal bubble is formed. This threshold does not change considerably when the confinement ratio of Cr = 4 is interested. Since the wall effects resist against the formation of toroidal bubble shape, the threshold increases when the confinement ratio falls below Cr = 4. Relatively large magnitude of Electro-capillary number Ec ≈ 1.9 is required for Cr = 2 to make the bubble form a toroidal shape.

Fig. 13 represents the terminal Reynolds number Re^* for different confinement ratios in variations of Electro-capillary number. It is stated earlier in Fig. 6 that when the bubble is pierced, the vertical rise velocity and consequently, the terminal Reynold number decreases considerably. Considering the terminal Reynolds number in two spectra of Electro-capillary number - Ec < 1.25 for non-pierced bubbles and Ec > 1.85 for toroidal bubbles - the terminal Reynolds number increases by incrementing the confinement ratio due to the effects of side boundary on the vertical rise velocity of the bubble. Moreover, by noticing the trend of terminal Reynolds number before the formation of the toroidal bubbles, it is observed that increments of Electro-capillary number lead to a slight in-

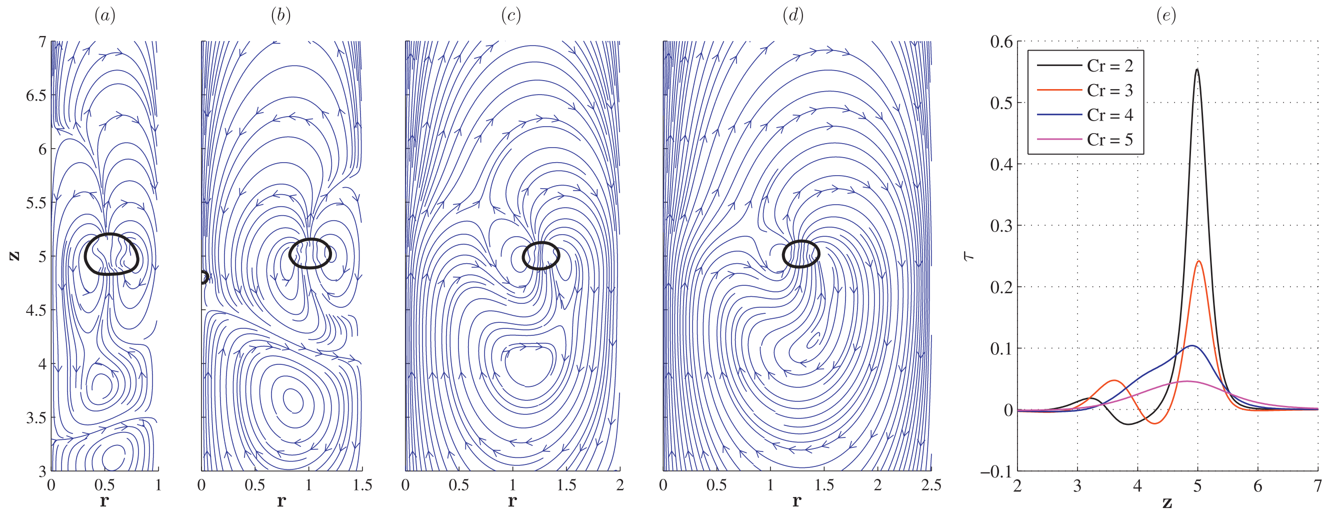

Fig. 10. The velocity streamlines and bubble shapes for Electro-capillary number of Ec = 2.5 and different confinement ratios; (a) Cr = 2, (b) Cr = 3, (c) Cr = 4, (d) Cr = 5 and (e) their corresponding wall shear stress; The bubbles are shown in a half domain for the moment when their centroids are at z = 5.

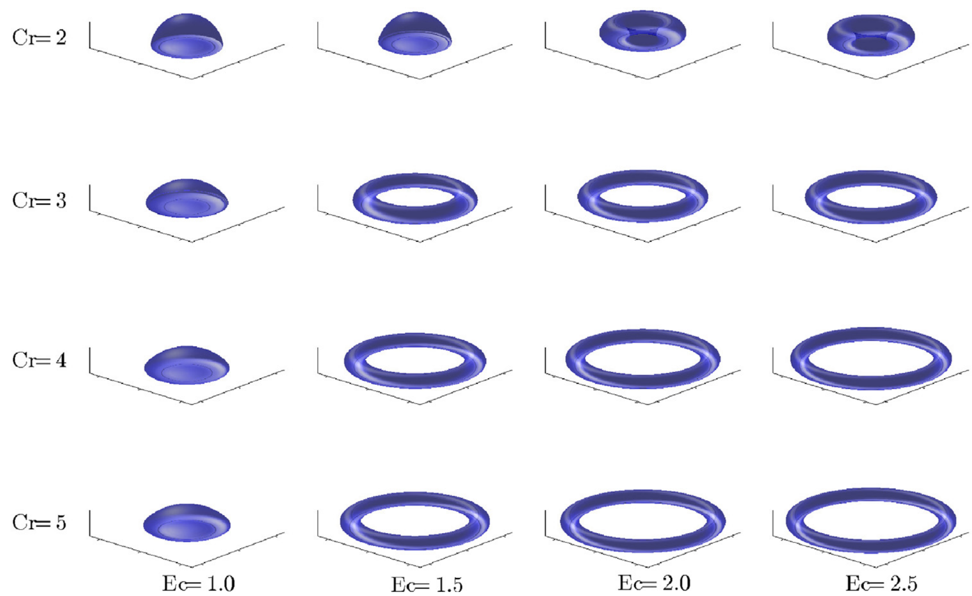

Fig. 11. Three-dimensional demonstration of terminal bubble shape for variations of Electro-capillary numbers and confinement ratios.

crease in the vertical rise velocity and consequently, the terminal Reynolds number for all confinement ratios. As it has been stated earlier, it is due to the formation of electric forces on the interface of the bubble which leads to a faster rise of the bubble in larger electric field strengths. After the formation of the toroidal bubble, however, increase in the Electro-capillary number does not influence the trend of terminal Reynolds number considerably. This indicates that the electric forces do not have a significant impact on the vertical rise velocity of the bubble after the formation of the toroidal shape.

Fig. 14 presents the variations of normalized diameter of the bubble ring D_r versus time after the bubble is pierced for some test cases in this study. The D_r is defined as the magnitude of the toroidal bubble diameter divided by the initial bubble diameter. The trend of D_r consists of two sections, one which has a steep slope showing the second transient stage of the bubble, and the other with a gentle slope indicating that the toroidal bubble gradually reaches its terminal state. During the second transient stage of rising, the toroid expands circumferentially and the bubble ring approaches the side boundary. This is due to the direction of the flow field of the surrounding fluid around the bubble that directs from the inner region of the bubble ring towards the side boundary. The flow field of the surrounding fluid around the bubble ring is motivated by the upward jet current, and can be seen in Fig. 10(d). It is observed that the pair vortices at the sides of the bubble ring develop leading to the gradual disappearance of the upward jet current. Considering the pair vortices, the vortex in the outer side of the bubble ring is found to be effective on the expansion of the bubble ring during the second transient stage. However, the expansion is ceased by the gradual strengthening of the inner vortex during the bubble rise, which is a turning point in the trend of the normalized diameter. Afterwards, the toroidal bubble reaches a plateau where the change in the normalized diameter is quite negligible. Since the development of the pair vortices around the bubble ring occurs earlier in time in smaller confinement ratios, reaching the plateau happens earlier for CE5 and CE6 cases. It should be noted that some oscillations are seen in the pattern of normalized diameter of the bubble ring for CE5 and CE6 cases which is due to the effects of the side boundary on the formation and strength of pair vortices around the bubble ring.

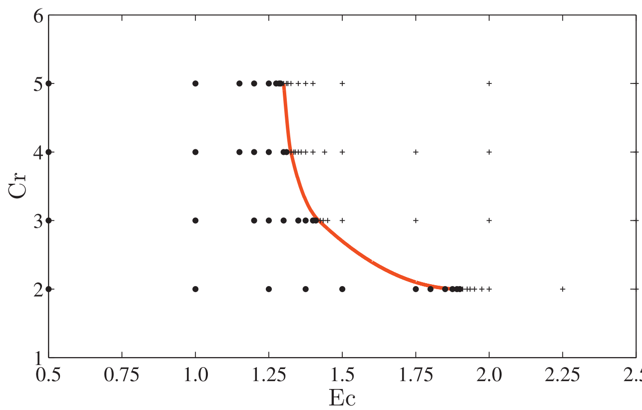

Fig. 12. The map of the test cases for variations of Electro-capillary numbers and confinement ratios simulated in present study; the circle marks indicate the cases wherein the rising bubble remains non-pierced while the plus marks represent the pierced cases. The red solid line indicates the transition region where the bubble pierces. (For interpretation of the references to colour in this figure legend, the reader is referred to the web version of this article.)

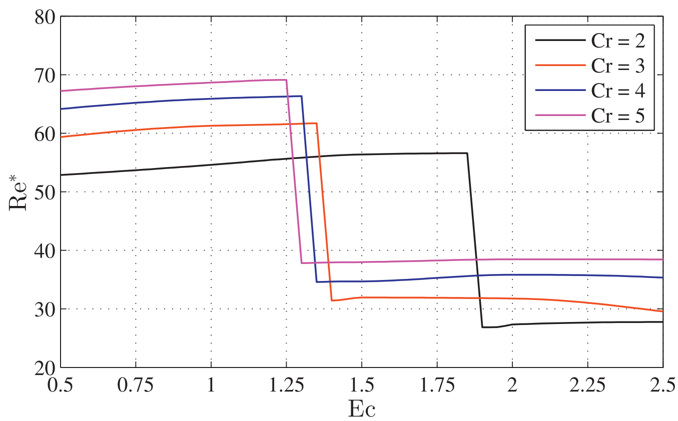

Fig. 13. Variations of Terminal Reynolds number as a function of Electro-capillary number for different confinement ratios.

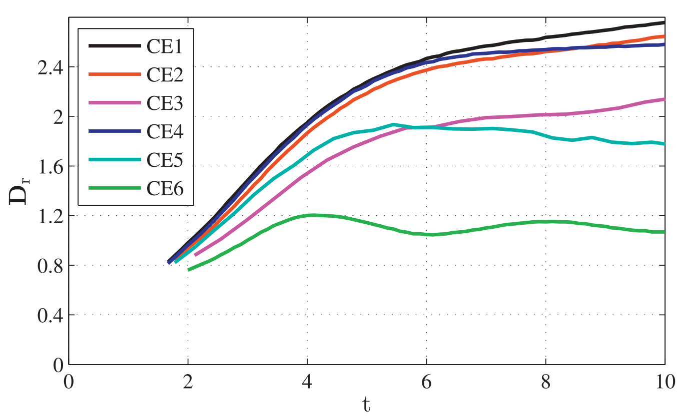

Fig. 14. The variations of normalized diameter of the bubble ring D_r in time for CE1 [Cr = 5, Ec = 2.5], CE2 [Cr = 5, Ec = 2], CE3 [Cr = 5, Ec = 1.5], CE4 [Cr = 4, Ec = 2.5], CE5 [Cr = 3, Ec = 2.5], and CE6 [Cr = 2, Ec = 2.5].

5. Conclusion

In this study, the combined effect of electrohydrodynamic forces and domain confinement is numerically studied for the formation of a toroidal bubble. The VOF method is used to capture the bubble interface. In order to implement the surface tension and electric forces, the Continuum Surface Force (CSF) and leaky dielectric models are used, respectively. The numerical tool is initially validated carefully for the bubble rising with experiments of Bhaga and Weber (1981) and numerical findings of Hua and Lou (2007). In regards to the electric forces, the accuracy of the numerical tool is compared for the bubble deformation problem with Taylor's theory (Saville, 1997) and numerical results of Lin et al. (2012).

In order to study the effect of domain confinement and electric force on the formation of a toroidal bubble, a case with the simulation conditions of $\mathrm{Re} = 100,\ \mathrm{Bo} = 50,\ \mathcal{D} = 0.001,\ \mathcal{V} = 0.01,\ \mathcal{C} = 0.001$, and $\mathcal{P} = 0.05$ is considered. Four confinement ratios, Cr = 2, 3, 4 and 5, are modeled and Electro-capillary number is adjusted to consider the effect of electric forces. It is found that both Electro-capillary number and confinement ratio are influential on the formation of the toroidal bubble. The bubble is pierced when the electric forces is sufficiently strong. The reason is that when the bubble is in the initial transient stage, the distance between the upper and bottom surfaces of the bubble decreases and then, the electric forces pierces the bubble. For smaller confinement ratios, larger Electro-capillary number is required to pierce the bubble. After the formation of a toroidal bubble, a secondary transient stage is observed. During the secondary transient stage, the vertical rise velocity of the bubble ring slightly decreases while the diameter of the bubble ring increases.

It is observed that in all confinement ratios, the bubble terminal Reynolds number increases with enhancement of electric forces up to the state where the bubble remains non-pierced. The formation of the toroidal bubble is followed by a sudden drop of almost 50 percent in bubble vertical rise velocity. Increasing the Electro-capillary number after the bubble piercing does not have a significant influence on the terminal Reynolds number. The terminal Reynolds number increases with increments of confinement ratio both before and after the formation of the toroidal bubble.

The study of the velocity streamlines revealed that after the formation of the toroidal bubble, a pair of vortices gently develops around the bubble ring resulting in gradual disappearance of the upward jet current. For smaller confinement ratios, the pair vortices develop right after the piercing, thus the upward jet current disappears earlier. Formation of the pair vortices results in the development of other complex vortices beneath the bubble ring.

Considering the wall shear stress, it is found that for all confinement ratios, the wall shear stress increases with increments of the Electro-capillary number. In larger confinement ratios, the magnitude of the wall shear stress is much smaller than the smaller confinements. Negative shear stress is found in some parts of the side wall elevations due to the existence of complex vortices formed after the piercing of the bubble, especially in smaller confinement ratio cases.

References

Al-Shamrani, A., James, A., Xiao, H., 2002. Separation of oil from water by dissolved air flotation. Colloids Surf., A 209, 15–26.
Bhaga, D., Weber, M., 1981. Bubbles in viscous liquids: shapes, wakes and velocities. J. Fluid Mech. 105, 61–85.
Bonometti, T., Magnaudet, J., 2006. Transition from spherical cap to toroidal bubbles. Phys. Fluids (1994-present) 18, 052102.
Brackbill, J., Kothe, D., Zemach, C., 1992. A continuum method for modeling surface-tension. J. Comput. Phys. 100, 335–354.
Chen, L., Garimella, S.V., Reizes, J.A., Leonardi, E., 1999. The development of a bubble rising in a viscous liquid. J. Fluid Mech. 387, 61–96.
Clift, R., Grace, J., Weber, M., 1978. Bubbles, Drops and Particles, 5. Academic Press, New York.
Eringen, A.C., Maugin, G.A., 2012. Electrodynamics of Continua I: Foundations and Solid Media. Springer Science & Business Media.
Feng, J.Q., Scott, T.C., 1996. A computational analysis of electrohydrodynamics of a leaky dielectric drop in an electric field. J. Fluid Mech. 311, 289–326.
Han, W., ZHANG, Z.-y., YANG, Y.-m., ZHANG, H.-s., 2010. Viscosity effects on the behavior of a rising bubble. J.Hydrodyn. Ser. B 22, 81–89.

Please cite this article as: A. Rahmat et al., The combined effect of electric forces and confinement ratio on the bubble rising, International Journal of Heat and Fluid Flow (2017), http://dx.doi.org/10.1016/j.ijheatfluidflow.2017.01.002

Hua, J., Lim, L.K., Wang, C.-H., 2008. Numerical simulation of deformation/motion of a drop suspended in viscous liquids under influence of steady electric fields. Phys. Fluids (1994-present) 20, 113302.
Hua, J., Lou, J., 2007. Numerical simulation of bubble rising in viscous liquid. J. Comput. Phys. 222, 769–795.
Kumar, P., Vanka, S., 2015. Effects of confinement on bubble dynamics in a square duct. Int. J. Multiphase Flow 77, 32–47.
Lin, Y., Skjetne, P., Carlson, A., 2012. A phase field model for multiphase electro-hydrodynamic flow. Int. J. Multiphase Flow 45, 1–11.
Mählmann, S., Papageorgiou, D.T., 2009. Buoyancy-driven motion of a two-dimensional bubble or drop through a viscous liquid in the presence of a vertical electric field. Theor. Comput. Fluid Dyn. 23, 375–399.
Mukundakrishnan, K., Quan, S., Eckmann, D.M., Ayyaswamy, P.S., 2007. Numerical study of wall effects on buoyant gas-bubble rise in a liquid-filled finite cylinder. Phys. Rev. E 76, 036308.
Pigeonneau, F., 2009. Mass transfer of a rising bubble in molten glass with instantaneous oxidation–reduction reaction. Chem. Eng. Sci. 64, 3120–3129.
Saville, D.A., 1997. Electrohydrodynamics: the taylor-melcher leaky dielectric model. Annu. Rev. Fluid Mech. 29, 27–64.
Takahashi, T., Miyahara, T., Nishizaki, Y., 1979. Separation of oily water by bubble column.. J. Chem. Eng. Jpn. 12, 394–399.
Taylor, G., 1966. Studies in electrohydrodynamics. i. the circulation produced in a drop by electrical field. In: Proceedings of the Royal Society of London A: Mathematical, Physical and Engineering Sciences, 291. The Royal Society, pp. 159–166.
Vizika, O., Saville, D., 1992. The electrohydrodynamic deformation of drops suspended in liquids in steady and oscillatory electric fields. J. Fluid Mech. 239, 1–21.
Wang, T., Li, H., Zhang, Y., Shi, D., 2015. Numerical simulation of bubble dynamics in a uniform electric field by the adaptive 3d-voset method. Numer. Heat Transfer, Part A 67, 1352–1369.
Yoon, H.Y., Koshizuka, S., Oka, Y., 2001. Direct calculation of bubble growth, departure, and rise in nucleate pool boiling. Int. J. Multiphase Flow 27, 277–298.
Zhang, J., Kwok, D.Y., 2005. A 2d lattice boltzmann study on electrohydrodynamic drop deformation with the leaky dielectric theory. J. Comput. Phys. 206, 150–161.